DE GRUYTER

Open Physics 2024; 22: 20240030

Research Article

Deman Zhang, Peng Deng, Ruijie Hou, Yongxing Song, Jingting Liu*, and Weibin Zhang

Study on cavitation and pulsation characteristics of a novel rotor-radial groove hydrodynamic cavitation reactor

https://doi.org/10.1515/phys-2024-0030
received January 05, 2024; accepted April 26, 2024

Abstract: Hydrodynamic cavitation is widely used in many fields such as water treatment, impact rock breaking, and food preparation. The performance of hydrodynamic cavitation is closely related to its internal flow field. In the present study, cavitation flow field was analyzed by computational fluid dynamics in the reactor. The cavitation performance of the rotor is evaluated under different operating conditions. The time frequency distribution of pressure pulsation is studied. The pressure increases at the connection point between the local low-pressure area and the mainstream low-pressure area. Cavitation bubbles collapsed at the tail end of the cavity to form a local void area. The blade frequency amplitude of pressure pulsation shows the significant periodic change. The blade frequency amplitude decreases along the flow direction. The effect of the fluid outlet led to the increase in the second-order harmonic frequency amplitude. The research results could provide theoretical support for the research of cavitation mechanism of cavitation equipment.

Keywords: hydrodynamic cavitation reactor, rotor-radial groove, cavitation bubbles, time frequency characteristics

Nomenclature

E	diffusivity
F_{vap}, F_{cond}	empirical coefficients of evaporation and condensation
G_{k}	turbulents kinetic energy term produced by buoyancy
k	turbulent kinetic energy
p	pressure
P_{v}	saturated vapor pressure of the medium at the working temperture
R_{B}	bubble radius
t	time
u_i, u_j	velocity in the x and y directions
u_i', u_j'	the time-average velocity in the x and y directions
x_i, x_j	coordinates in the x and y directions
α_{nuc}	volume fraction of nucleation points
α_{v}	volume fraction of steam
ρ_{v}	vapor density
ε	turbulent pulsation rate
σ_k, σ_ε	turbulent Prandtl numbers of the k equation and ε equation
μ	fixed dynamic viscosity
μ_{t}	turbulent dynamic viscosity
ρ	density
μ	dynamic viscosity

1 Introduction

Hydrodynamic cavitation is a process in which cavitation bubbles are generated, expanded, and finally collapsed when the local pressure is lower than the saturated vapor pressure. Local hot spots (2,300–4,600 K) [1], shock waves, shear stresses (100–5,000 bar) [2], and strong oxidizing hydroxyl radicals and hydrogen peroxide radicals [3] are generated when the cavitation bubbles collapse. The impeller of hydraulic machinery was destroyed by the cavitation bubbles collapse [4]. The intensification of vibration/noise and performance degradation may

---

*** Corresponding author: Jingting Liu,** School of Mechanical Engineering, Shandong University, Jinan 250061, China, e-mail: liujingting@sdu.edu.cn

Deman Zhang, Peng Deng: Wuhan Second Ship Design and Research Institute, Wuhan 430205, Hubei, China

Ruijie Hou, Yongxing Song: School of Thermal Engineering, Shandong Jianzhu University, Jinan 250101, China

Weibin Zhang: Key Laboratory of Fluid and Power Machinery (Xihua University), Ministry of Education, Chengdu 610039, China

lead to damage to water conservancy buildings in severe cases, such as damage to the bottom outlet of the dam [5,6].

With the rapid development of modern industry, hydrodynamic cavitation technology has been widely applied in the industrial field. It is feasible and efficient to apply hydrodynamic cavitation technologies in industry and life [7,8]. At the same time, hydraulic cavitation can be applied to biomass pretreatment to improve the efficiency of anaerobic digestion and protect the environment [9]. In previous research on hydrodynamic cavitation applications, venturi tubes and orifice plates were widely used to generate cavitation [10]. It also can cause significant pressure loss and energy dissipation [11]. In addition, venturi tubes and orifice plates are easy to corrosion and blockage. It is difficult to achieve widespread application. Various rotary hydrodynamic cavitation reactors have been proposed to address this phenomenon [12]. The mechanism, design, and application of various hydraulic cavitation reactors are analyzed and compared by some researchers [13]. The cavitation is generated by the interference effects between the stator and rotor, and the shear effects of the rotor in the rotation hydrodynamic cavitation reactor [14]. The rotation hydrodynamic cavitation reactor has the characteristics of high energy efficiency and good economic benefits, which has extremely high application value [15,16]. Petkovšek *et al.* [17] studied the cavitation effect of a rotation hydrodynamic cavitation reactor composed of two rotors with opposite radial grooves. The results showed that new cavitation was formed in the shear cavitation. Sun *et al.* [18,19] studied the cavitation flow characteristics of representative interactive hydraulic cavitation reactors. The mechanism and development process of cavitation were analyzed by experimental flow visualization and numerical simulation methods. Badve *et al.* [11] proposed a new type of hydraulic cavitation reactor. The reactor consists of a grooved rotor and stator. A strong shear cavitation occurs at the groove when liquid enters and exits the groove at high speed. The internal hydrodynamic cavitation of the centrifugal pump was analyzed. The flow pattern was judged to obtain the optimal inducer angle for hydraulic cavitation performance by numerical simulation.

For the numerical simulation of hydraulic cavitation, it is usually necessary to solve complex partial differential equations. These complex partial differential equations usually cannot be solved analytically, so they can only be solved numerically. Some researchers use B-spline function to solve complex equations numerically, and the results show that this method has better stability and convergence than other methods [20–22]. Tassaddiq *et al.* [23] also used B-spline function to solve viscoelastic flow and hydrodynamic stability problems, and the results show that this method is more efficient. Khalid *et al.* [24] used polynomial and non-multinomial splines to solve the fluid dynamics stability problem, and compared with other methods, the results show that the solution accuracy is higher with polynomial and non-multinomial splines. Some researchers have theorized how to solve similar problems [25]. There are many existing computational models for hydraulic cavitation. Ranade has summarized and compared various computational models of various hydraulic cavitation reactors, and made prospects, which provides a useful perspective for the design and optimization of hydrodynamic cavitation applications [26].

In our previous research work, an advanced rotor radial gap hydraulic cavitation reactor was proposed. The reactor has excellent cavitation disinfection performance [27,28]. Disinfection rate of 93.3% can be achieved with 15 min for 15 L simulated effluent. The hydrodynamic cavitation reaction is mainly based on the shear cavitation effect generated by the high-speed rotor in the hydrodynamic cavitation reactor. The cavitation effect in the rotor region periodically collapses to produce powerful cavitation effect. On the other hand, the rotor region induces cavitation bubbles into the stator cavitation unit [29]. Therefore, the cavitation flow field in the rotor plays an important role in improving the cavitation performance of the reactor.

In this study, the cavitation characteristics of the rotor-radial groove (RRG) hydrodynamic cavitation reactor were studied by the Realizable k–ε turbulence model and the Zwart (Zwart-Gerber-Belamri) cavitation model. Numerical calculations were conducted on the unsteady cavitation flow field at different speeds. The interaction relationship between cavitation and pressure fluctuation characteristics was studied. The development of internal pressure pulsation in the reactor and the influence of rotational speed on the cavitation performance of the rotor impeller region were analyzed. The theoretical basis for the cavitation mechanism and the reference for the design and optimization were provided.

This study is organized as follows. The modeling is proposed in Section 2. Section 3 describes the numerical method including meshing and solver. The cavitation performance of the reactor rotor area under different operating conditions is evaluated, and the time-frequency distribution of pressure pulsation in the reactor rotor region is studied in Section 4. Finally, the conclusions are drawn in Section 5.

2 Modeling

2.1 Governing equations

This simulation method is based on the Reynold-averaged Navier–Stokes control equation to solve the turbulent flow field in the RRG hydrodynamic cavitation reactor [30,31]. The continuity equations and momentum equations are as follows:

Continuity equation:

$$\frac{\partial \rho}{\partial t} + \frac{\partial}{\partial x_i}(\rho u_i) = 0. \tag{1}$$

Momentum equation:

$$\frac{\partial}{\partial t}(\rho u_i) + \frac{\partial}{\partial x_i}(\rho u_i u_j) = -\frac{\partial p}{\partial x_i} + \frac{\partial}{\partial x_j}(\mu \frac{\partial u_i}{\partial x_j} - \rho u_i' u_j'), \tag{2}$$

where ρ is the density, kg/m^3; p is the pressure, Pa; μ is the dynamic viscosity, N s/m^2; u_i' and u_j' are the time-average velocity in the x and y directions, m/s; t is the time, s; u_i and u_j are the velocity in the x and y directions, m/s; and x_i and x_j are the coordinates in the x and y directions.

2.2 Cavitation model

The development of bubbles was calculated using the Zwart (Zwart-Gerber-Belamri) cavitation model based on the Ray–Plesset equation, assuming the same bubble radius [32,33].

When $P < P_v$,

$$R_e = F_{\text{vap}} \frac{3\alpha_{\text{nuc}}(1 - \alpha_v)\rho_v}{R_B} \sqrt{\frac{2(P_v - P)}{3\rho_1}}, \tag{3}$$

and when $P > P_v$,

$$R_c = F_{\text{cond}} \frac{3\alpha_v \rho_v}{R_B} \sqrt{\frac{2(P - P_v)}{3\rho_1}}, \tag{4}$$

where F_{vap} and F_{cond} denote the empirical coefficients of evaporation and condensation ($F_{\text{vap}} = 50$, $F_{\text{cond}} = 0.01$). P is the flow field pressure, Pa; P_v is the saturated vapor pressure of the medium at the working temperature, Pa; α_{nuc} is the volume fraction of nucleation points; α_v is the volume fraction of steam; ρ_1 is the flow field density, kg/m^3; ρ_v is the vapor density, kg/m^3; andR_B is the bubble radius, m. The evaporation process is calculated by Eq. (3). F_{vap} is the evaporation empirical coefficient. The condensation process is calculated by Eq. (4). F_{cond} is the condensation empirical coefficient.

2.3 Turbulence model

The turbulence model plays an important role on the cavitation flow field of the reactor. The selection of turbulence models is an important factor affecting the accuracy of cavitation flow field [34]. The realizable k–epsilon (k–ε) model was applied for numerical calculation. For the blind hole jet process, the realizable k–ε model is more accurate than other models. The correction formula for turbulent viscosity was added to the realizable k–ε model. The model takes into account the impact of turbulent viscosity on average rotation. It can provide more accurate calculations for this process [35,36].

For the realizable k–ε model of incompressible fluids, the equations for k and ε are expressed by Eqs. (5) and (6).

$$\frac{\partial(\rho k)}{\partial t} + \frac{\partial(\rho k u_i)}{\partial x_i} = \frac{\partial}{\partial x_j}\left[\left(\mu + \frac{\mu_t}{\sigma_k}\right)\frac{\partial k}{\partial x_j}\right] + G_k - \rho\varepsilon, \tag{5}$$

$$\frac{\partial(\rho \varepsilon)}{\partial t} + \frac{\partial(\rho \varepsilon u_i)}{\partial x_i} = \frac{\partial}{\partial x_j}\left[\left(\mu + \frac{\mu_t}{\sigma_k}\right)\frac{\partial \varepsilon}{\partial x_j}\right] + \rho C_1 E \varepsilon - \rho C_2 \frac{\varepsilon^2}{k + \sqrt{v\varepsilon}}, \tag{6}$$

where ε is the turbulent pulsation rate; C_1 and C_2 are the constants; σ_k and σ_ε are the turbulent Prandtl numbers of the k equation and ε equation; G_k is the turbulent kinetic energy term produced by buoyancy; v is the turbulent velocity, m/s; μ is the fixed dynamic viscosity, N s/m^2; μ_t is the turbulent dynamic viscosity, N s/m^2; E is the diffusivity; k is the turbulent kinetic energy, m^2/s^2; and ρ is the turbulent density, kg/m^3.

2.4 Geometric model

The RRG hydrodynamic cavitation reactor consists of rotor, stator, and casing. The rotor is the semi open impeller structure with multiple blind holes, which can promote the development of impeller attachment cavitation. The stator is a cylindrical entity with multiple rectangular gaps. The RRG would produce a shear separation zone based on Kelvin–Helmholtz instability to promote the development of shear cavitation. The RRG is arranged on the stator. The RRG can generate large pressure pulsations based on a previously patented blind hole design. Specifics of the RRG hydrodynamic cavitation reactor structure and definitions of RRG can be found in our previous works [17,18]. The shell is the volute type structure. The liquid flows into the gap between the stator and rotor through the inlet. The liquid flow was thrown out through high-speed rotation of the rotor. It has been verified that there is a high-strength hydrodynamic cavitation effect in the reactor. Figure 1 shows the model diagram of the RRG hydrodynamic cavitation reactor.

3 Numerical method

3.1 Boundary condition

The volume of fluid model was applied to predict multiphase flow in the reaction. The model inlet adopts velocity inlet boundary conditions. The model outlet adopts free pressure outlet boundary conditions. The inlet speed is specified as 0.97 m/s. The wall temperature remains constant at 300 K.

3.2 Mesh of modeling

The geometric modeling is meshed with mesh size of 0.08 cm and mesh number of 2,875,071. The boundary layer at the wall was densified. Polyhedral grids were applied to mesh the computational domain of reactors. To improve the calculation accuracy and save calculation time, four expansion layers were formed in the interaction area between the stator and rotor. The rotor area adopts sliding walls and sliding grids. Table 1 shows the grid independency.

3.3 Location of monitoring points

In order to study the pressure fluctuation characteristics at different positions of the RRG hydrodynamic cavitation reactor, eight monitoring points were arranged inside. The monitoring points P1–P8 are uniformly distributed on the middle section of the reactor. P8 is located in the position of the volute tongue. The specific location of the monitoring points is shown as Figure 2.

3.4 Signal processing methods

In this study, the time-frequency analysis technology of wavelet transform was used to identify the central

Table 1: Grid independency

Mesh size (cm)	Pressure (hPa)	Mesh number
0.06	−293.0	5,589,651
0.08	−292.8	2,875,071
0.10	−296.5	1,572,897
0.12	−299.6	1,024,077
0.14	−305.1	705,183

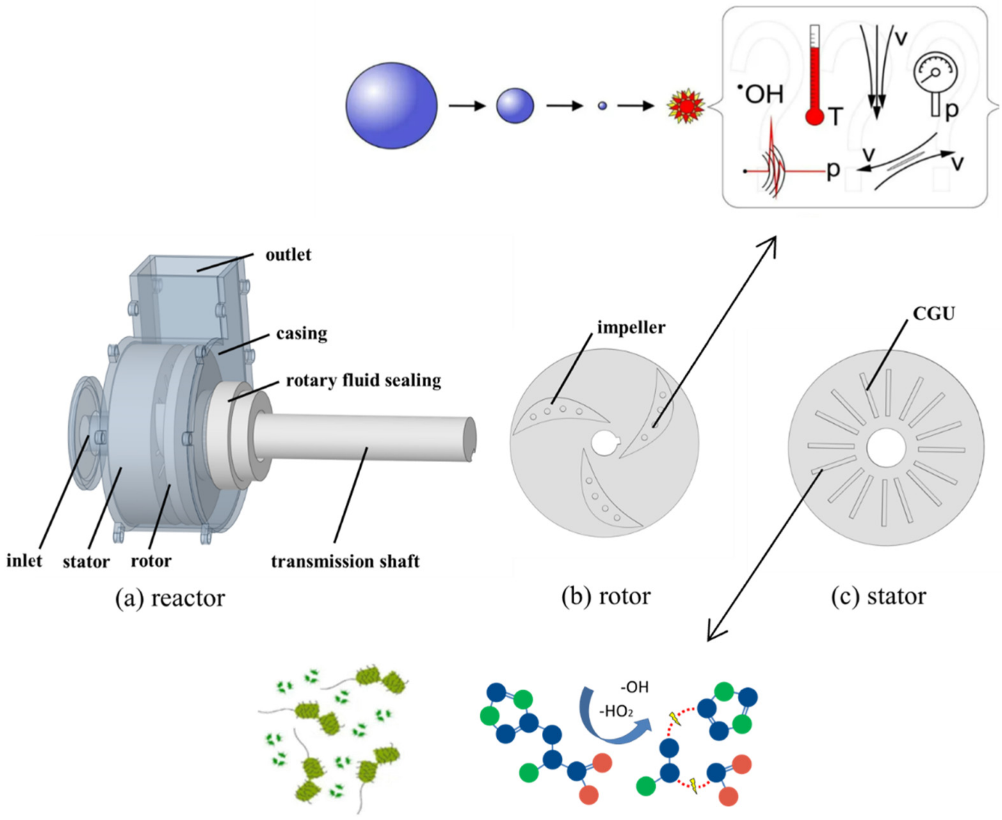

Figure 1: Schematic diagram of the RRG hydrodynamic cavitation reactor. (a) Reactor, (b) rotor, and (c) stator.

frequency band of pressure signal. Wavelet transform is an important analysis method in signal processing. Wavelet transform can simultaneously display the effective information of signals in both time and frequency domains. It has high accuracy for low-frequency signals. The frequency of pressure pulsation is mostly between 0 and 2,000 Hz in the reactor. A wavelet transform could accurately and effectively analyze and process the signals [37].

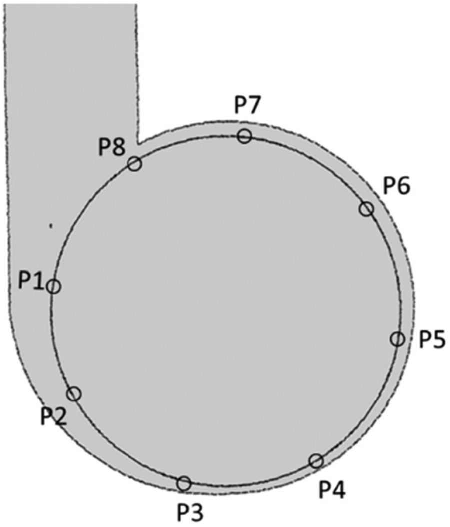

Figure 2: Location of monitoring points.

4 Results and discussion

4.1 Cavitation characteristics in rotor

The cavitation of the RRG hydrodynamic cavitation reactor was generated by the shear cavitation of the rotor, the cavitation development presented an obvious periodicity. The development of cavitation in rotor (vapor phase velocity) is depicted in Figure 3. Figure 4 shows the location of the rotor.

At 0 ms, cavitation occurs at the inlet of the suction surface of the rotor. The closer to the back of the rotor, the greater the gas phase volume fraction. Local vacuum area is formed on the back of the rotor. At 2.6306 ms, partial bubbles break at the tail end of the cavity. It split with the mainstream cavitation region to form a local cavitation region. Due to the influence of the fluid outlet, the area of the cavitation area on the back of the rotor decreased. At the same time, the local cavitation bubbles on the back of the blade collapses. From 2.6306 to 7.8918 ms, the cavitation enters the stage of recovery and development in the rotor. The cavitation area increased in the rotor. Local cavitation area appeared on the back of the rotor. From 7.8918 to 13.153 ms, the cavitation in the rotor area is in a stable state. The cavitation area inside the rotor decreases first, then increases, and finally stabilizes over time.

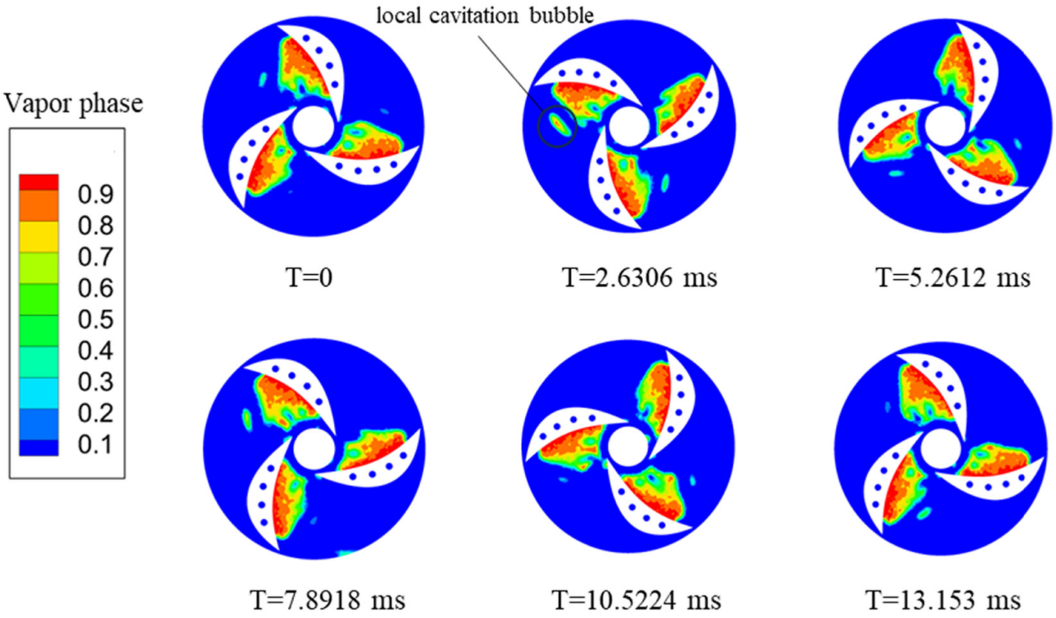

Figure 3: The cavitation development in rotor in one cycle.

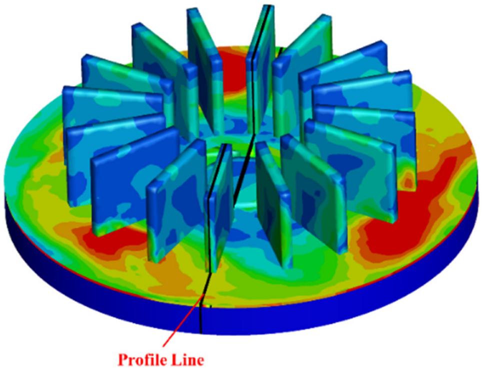

Figure 4: The bird's-eye view of the profile location.

The pressure distribution affects the cavitation morphology of the RRG hydrodynamic cavitation reactor. Figure 5 depicts the development of cavitation in optimized rotor (pressure). The low-pressure area appears on the back of the rotor suction surface and entrance circumference. The minimum pressure can reach 102,000 Pa. The low-pressure zone corresponds to the cavitation zone. This explains the reason for the formation of localized cavitation areas. Local low-pressure area leads to the formation of local cavitation zone. The pressure increases at the connection point between the local low-pressure area and the mainstream low-pressure area. Cavitation breaks at the tail end of the cavity to form a local void area. From 0 to 2.6306 ms, the low-pressure area decreases due to the fluid outlet. The local low-pressure area disappears. The pressure increases to make the local low-pressure area disappear.

In the RRG hydrodynamic cavitation reactor, shear cavitation is generated based on the shear effect of high-speed rotor rotation. Vorticity is an important factor in measuring the strength of shear separation. In this study, the vorticity is used as a measure of the strength of shear separation. The development of cavitation in rotor (vorticity) is shown in Figure 6. The high vorticity zone is concentrated at the inlet of the impeller suction surface and the circumference of the rotor inlet. The high vorticity region corresponds to the region where cavitation occurred. The shear cavitation bubbles generated by high-speed rotation of the rotor is the main cavitation form in the rotor. The vorticity can reach up to 8,000 in high vorticity areas. From 2.6306 to 5.2612 ms, the rotor turns to the fluid outlet. The vorticity decreases to 1,000 on the back of the rotor rapidly. The vorticity decreases in a strip shape along the rotor wake. The vorticity shows the trend of high in the middle and low at both ends. Therefore, the degree distribution of vorticity is an important reason for the formation and disappearance of local cavitation bubble areas.

4.2 Time-frequency characteristics of pressure pulsation

The cavitation intensity is high when the rotor speed is 4,200 rpm. The pressure pulsation signal can better reflect

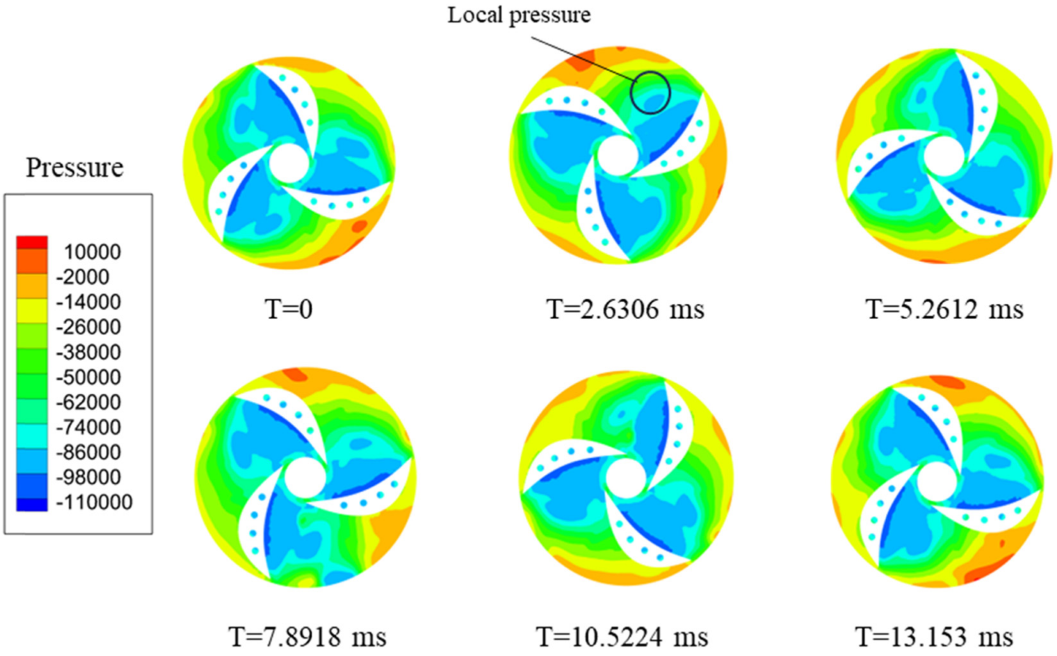

Figure 5: The pressure development in rotor in one cycle.

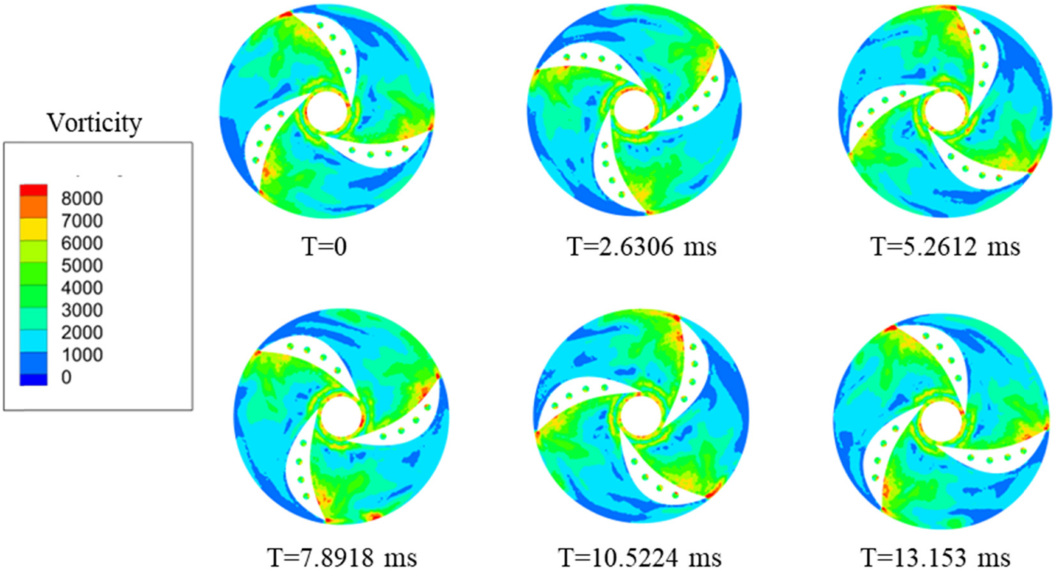

Figure 6: The vorticity development in rotor in one cycle.

the relationship between cavitation and time-frequency pressure pulsation. The cavitation intensity is high. And its pressure fluctuation signal can better reflect the relationship between cavitation and time-frequency pressure fluctuation when the rotor speed is 3,600 and 4,200 rpm. In this study, the time-frequency characteristics of monitoring point pressure fluctuation signal were analyzed under the steady state condition, which was based on wavelet transform when the rotor speed is 4,320 rpm. The time-frequency diagram of pressure pulsation at each point is shown in Figure 7. The amplitude of pressure pulsation at each monitoring point was mainly distributed in the range of 0–1,500 Hz. The amplitude was concentrated in the blade frequency, double harmonic frequency, and triple harmonic frequency.

The time-frequency distribution at a speed of 3,300 rpm without cavitation is shown in Figure 7. The flow direction inside the reactor is P8–P1. The blade frequency amplitude inside the reactor shows two decreasing stages. The first descent stage is the flow exit stage, which is the P8–P5 stage. From P8–P5, the blade frequency amplitude decreased by 108,912 Pa. This is because of the influence of the fluid outlet, the blade frequency amplitude of P8 has an instantaneous increase. The blade frequency amplitude of P1–P8 increased from 189,698 to 62,606 Pa. The second descending stage is the flow inlet stage, which is the P5–P1 stage. From P5–P1, the blade frequency amplitude decreased by 86,100. In summary, the blade frequency amplitude of pressure pulsation shows significant periodic change. The blade frequency amplitude decreases along the flow direction. The effect of the fluid outlet led to the increase in the second-order harmonic frequency amplitude.

Similar to 3,300 rpm operating conditions, the amplitude of 4,200 rpm (shown in Figure 8) is concentrated in blade frequency, double harmonic frequency, and triple harmonic frequency. Unlike low-speed operating conditions, the amplitudes of each frequency are enhanced to varying degrees at 4,200 rpm. The development of cavitation leads to the increase in blade frequency amplitude of pressure pulsation. The specific time-frequency distribution is opposite to low-speed conditions. The blade frequency amplitude of P8–P6 gradually increased from 177,275 to 181,137. The amplitude of blade frequency of P4–P1 gradually increased from 171,466 to 275,066. This is because of the enhancement of broadband pressure pulsation caused by cavitation. It led to the gradual increase in blade frequency amplitude of pressure pulsation along the flow direction.

5 Conclusion

In the present study, the cavitation flow field in the rotor region of the reactor was analyzed by computational fluid dynamics. The cavitation characteristics of the RRG hydrodynamic cavitation reactor were studied by the realizable k–ε turbulence model and the Zwart cavitation model. The cavitation performance of the reactor rotor area under different operating conditions was evaluated. The time-frequency distribution of pressure pulsation in the reactor rotor region was studied. The following conclusions could be drawn from the present investigation.

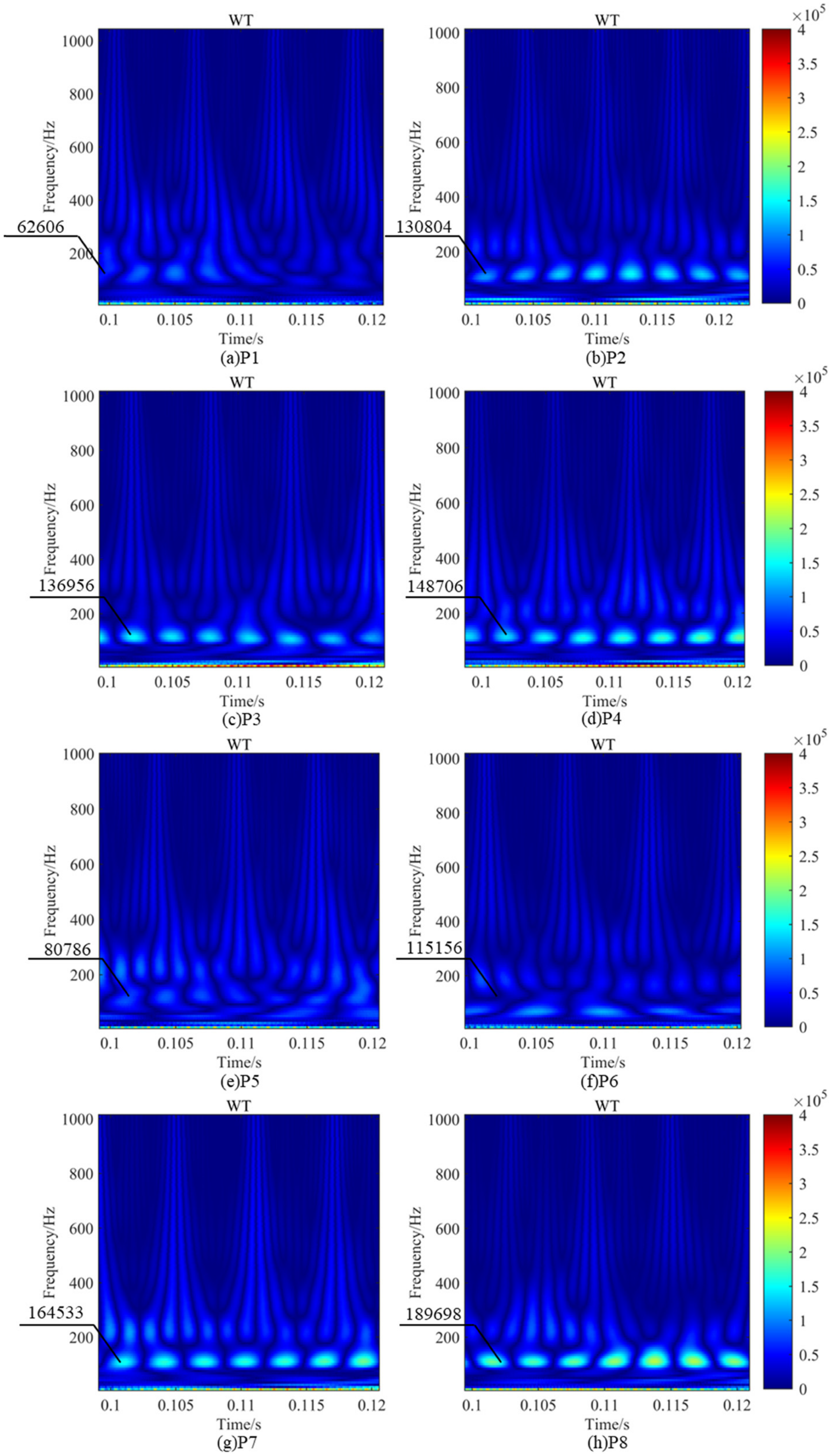

Figure 7: The time-frequency characteristics of pressure pulsation at 3,300 rpm. (a) P1, (b) P2, (c) P3, (d) P4, (e) P5, (f) P6, (g) P7, (h) P8.

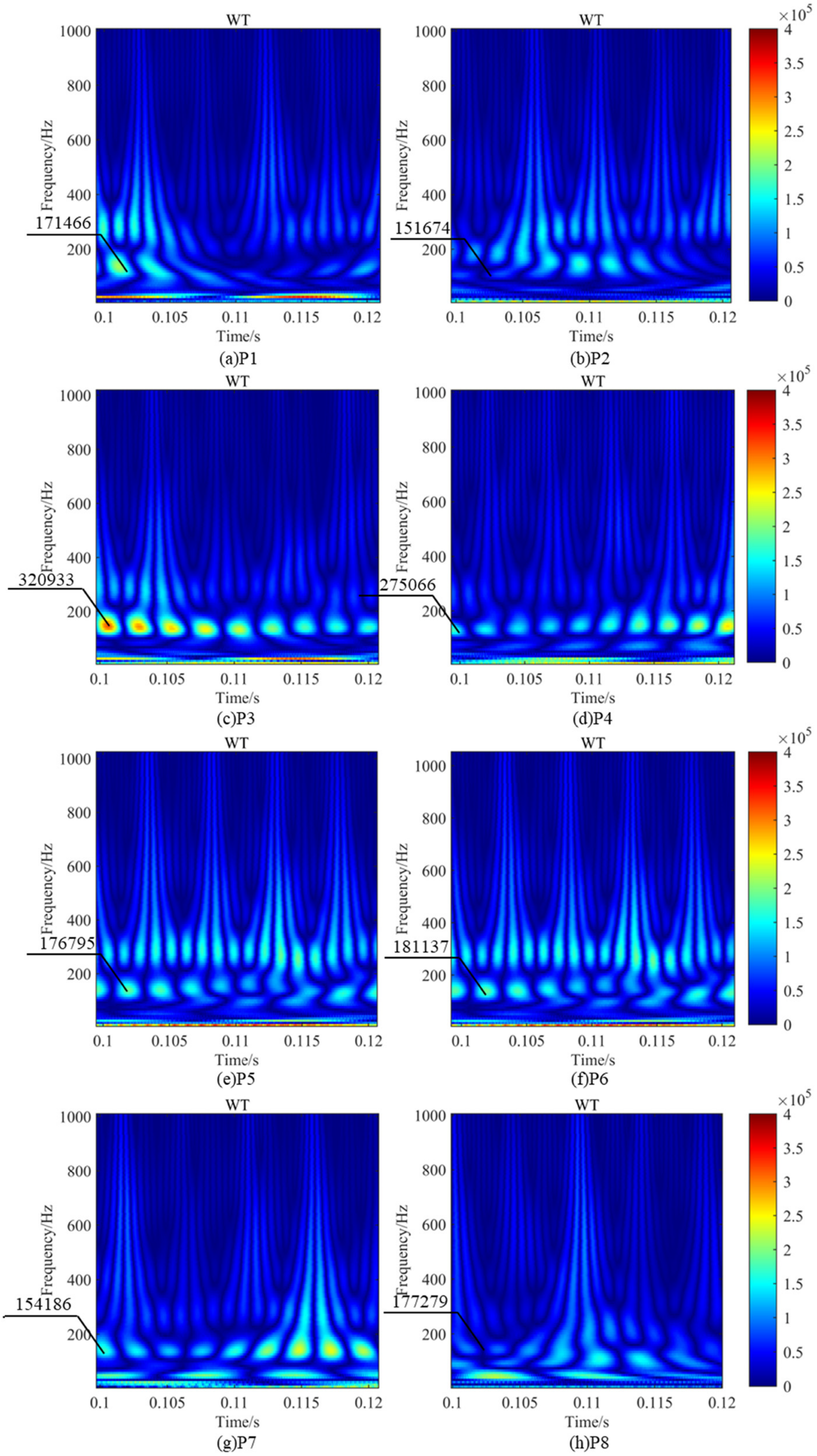

Figure 8: The time-frequency characteristics of pressure pulsation at 4,200 rpm. (a) P1, (b) P2, (c) P3, (d) P4, (e) P5, (f) P6, (g) P7, (h) P8.

- Local low-pressure area leads to the formation of local cavitation zone. The pressure increases at the connection point between the local low-pressure area and the mainstream low-pressure area. Cavitation bubbles collapsed at the tail end of the cavity to form a local void area.
- The shear cavitation bubble generated by high-speed rotation of the rotor is the main cavitation form in the rotor.
- The blade frequency amplitude of pressure pulsation shows the significant periodic change. The blade frequency amplitude decreases along the flow direction. The effects of the fluid outlet led to the increase in the second-order harmonic frequency amplitude.
- The specific time-frequency distribution is opposite to low-speed conditions. The blade frequency amplitude of P8–P6 gradually increased from 177,275 to 181,137. The amplitude of blade frequency of P4–P1 gradually increased from 171,466 to 275,066. This is because the enhancement of broadband pressure pulsation caused by cavitation. It led to the gradual increase in blade frequency amplitude of pressure pulsation along the flow direction.

There are some shortcomings in the extraction of cavitation signals in this study. The influence of flow induced pressure on cavitation pressure signals is not considered. In future work, the cavitation model should be further revised to establish more effective signal processing methods for cavitation pressure pulsation to improve the accuracy of numerical simulation.

Acknowledgments: The authors acknowledge the support by the National Natural Science Foundation of China (No. 52006126), the Open Research Subject of Key Laboratory of Fluid and Power Machinery (Xihua University), Ministry of Education (grant number LTDL-2023007) and the Natural Science Foundation of Shandong Province (No. ZR2020QE193, No. ZR2021QE157).

Funding information: This work was supported by the National Natural Science Foundation of China (No. 52006126), the Natural Science Foundation of Shandong Province (No. ZR2020QE193 and No. ZR2021QE157) and the Open Research Subject of Key Laboratory of Fluid and Power Machinery (Xihua University), Ministry of Education (Grant number LTDL-2023007).

Author contributions: Deman Zhang contributed toward conducting the experiments, resource acquisition, data analysis, and writing the original draft. Peng Deng contributed toward the investigation, data analysis, and writing the original draft. Ruijie Hou contributed toward data analysis and writing – review and reediting. Yongxing Song contributed toward resource acquisition, and data analysis. Jingting Liu contributed toward the methodology, resource acquisition, and writing – review and reediting. Weibin Zhang contributed toward developing the project administration and supervision. All authors have accepted responsibility for the entire content of this manuscript and approved its submission.

Conflict of interest: The authors state no conflict of interest.

Data availability statement: The data that support the findings of this study are available from the corresponding author upon reasonable request.

References

[1] Rae J, Ashokkumar M, Eulaerts O, Von Sonntag C, Reisse J, Grieser F. Estimation of ultrasound induced cavitation bubble temperatures in aqueous solutions. Ultrason Sonochem. 2005;12(5):325–9.

[2] Sun X, You W, Xuan X, Ji L, Xu X, Wang G, et al. Effect of the cavitation generation unit structure on the performance of an advanced hydrodynamic cavitation reactor for process intensifications. Chem Eng J. 2021;412:128600.

[3] Wang X, Jia J, Wang Y. Combination of photocatalysis with hydrodynamic cavitation for degradation of tetracycline. Chem Eng J. 2017;315:274–82.

[4] Song Y, Hou R, Zhang W, Liu J. Hydrodynamic cavitation as an efficient water treatment method for various sewage: A review. Water Sci Technol. 2022;86(2):302–20.

[5] Fadaei Kermani E, Barani GA, Ghaeini-Hessaroeyeh M. Prediction of cavitation damage on spillway using K-nearest neighbor modeling. Water Sci Technol. 2015;71(3):347–52.

[6] Barik AJ, Gogate PR. Hybrid treatment strategies for 2,4,6-trichlorophenol degradation based on combination of hydrodynamic cavitation and AOPs. Ultrason Sonochem. 2018;40:383–94.

[7] Wang K, Jin RY, Qiao YN, He ZD, Wang Y, Wang XJ. The removal of Rhodamine B by H_2O_2 or ClO_2 combined with hydrodynamic cavitation. Water Sci Technol. 2019;80(8):1571–80.

[8] Pandya K, Anantha Singh TS, Kodgire P, Simon S. Combined ultrasound cavitation and persulfate for the treatment of pharmaceutical wastewater. Water Sci Technol. 2022;86(9):2157–74.

[9] Abdrashitov A, Gavrilov A, Marfin E, Pancheko V, Kovalev A, Bolshev V, et al. Cavitation reactor for pretreatment of liquid agricultural waste. Agriculture. 2023;13(6):1218.

[10] Badve MP, Gogate PR, Pandit AB, Csoka L. Hydrodynamic cavitation as a novel approach for delignification of wheat straw for paper manufacturing. Ultrason Sonochem. 2014;21(1):162–8.

[11] Badve M, Gogate P, Pandit A, Csoka L. Hydrodynamic cavitation as a novel approach for wastewater treatment in wood finishing industry. Sep Purif Technol. 2013;106:15–21.

[12] Cerecedo LM, Dopazo C, Gomez-Lus R. Water disinfection by hydrodynamic cavitation in a rotor-stator device. Ultrason Sonochem. 2018;48:71–8.

[13] Zheng HX, Zheng Y, Zhu JS. Recent developments in hydrodynamic cavitation reactors: Cavitation mechanism, reactor design, and applications. Engineering. 2022;19:180–98.

[14] Li M, Bussonnière A, Bronson M, Xu Z, Liu Q. Study of Venturi tube geometry on the hydrodynamic cavitation for the generation of microbubbles. Miner Eng. 2019;132:268–74.

[15] Saharan VK, Pandit AB, Satish Kumar PS, Anandan S. Hydrodynamic cavitation as an advanced oxidation technique for the degradation of Acid Red 88 dye. Ind Eng Chem Res. 2012;51(4):1981–9.

[16] Ikai H, Nakamura K, Shirato M, Kanno T, Iwasawa A, Sasaki K, et al. Photolysis of hydrogen peroxide, an effective disinfection system via hydroxyl radical formation. Antimicrobial Agents Chemother. 2010;54(12):5086–91.

[17] Petkovšek M, Zupanc M, Dular M, Kosjek T, Heath E, Kompare B, et al. Rotation generator of hydrodynamic cavitation for water treatment. Sep Purif Technol. 2013;118:415–23.

[18] Sun X, Xuan X, Song Y, Jia X, Ji L, Zhao S, et al. Experimental and numerical studies on the cavitation in an advanced rotational hydrodynamic cavitation reactor for water treatment. Ultrason Sonochem. 2021;70:105311.

[19] Sun X, Liu J, Ji L, Wang G, Zhao S, Yoon JY, et al. A review on hydrodynamic cavitation disinfection: The current state of knowledge. Sci Total Environ. 2020;737:139606.

[20] Khalid N, Abbas M, Iqbal MK, Baleanu D. A numerical algorithm based on modified extended B-spline functions for solving time-fractional diffusion wave equation involving reaction and damping terms. Adv Differ Equ. 2019;2019(1):1.

[21] Akram T, Abbas M, Riaz M, Ismail A, Ali N. An efficient numerical technique for solving time fractional Burgers equation. Alex Eng J. 2020;59(4):2201–20.

[22] Khalid N, Abbas M, Iqbal M, Baleanu D. A numerical investigation of Caputo time fractional Allen–Cahn equation using redefined cubic B-spline functions. Adv Differ Equ. 2020;2020(1):158.

[23] Tassaddiq A, Khalid A, Naeem M, Ghaffar A, Khan F, Karim S, et al. A new scheme using cubic B-spline to solve non-linear differential equations arising in visco-elastic flows and hydrodynamic stability problems. Mathematics. 2019;7(11):1078.

[24] Khalid A, Ghaffar A, Naeem M, Nisa K, Baleanu D. Solutions of BVPs arising in hydrodynamic and magnetohydro-dynamic stability theory using polynomial and non-polynomial splines. Alex Eng J. 2021;60(1):941–53.

[25] Singh B, Nisar KS. Thermal instability of magnetohydrodynamic couple stress nanofluid in rotating porous medium. Numer Methods Partial Differ Equ. 2023;39(6):4454–67.

[26] Ranade VV. Modeling of hydrodynamic cavitation reactors: Reflections on present status and path forward. ACS Eng Au. 2022;2(6):461–76.

[27] Song Y, Hou R, Liu Z, Liu J, Zhang W. Cavitation characteristics analysis of a novel rotor-radial groove hydrodynamic cavitation reactor. Ultrason Sonochem. 2022;86:106028.

[28] Hou R, Song Y, Liu J, Zhang L, Zhang M, Sun X. Experimental and numerical investigation on the disinfection characteristics of a novel rotor-radial groove hydrodynamic cavitation reactor. Process Saf Environ Prot. 2023;169:260–9.

[29] Farhadi A, Mayrhofer A, Tritthart M, Glas M, Habersack H. Accuracy and comparison of standard k-ϵ with two variants of k-ω turbulence models in fluvial applications. Eng Appl Comput Fluid Mech. 2018;12(1):216–35.

[30] Menter FR, Kuntz M, Langtry R. Ten years of industrial experience with the SST turbulence model. Turbul Heat Mass Transf. 2003;4(1):625–32.

[31] Zwart PJ, Gerber AG, Belamri T. A two-phase flow model for predicting cavitation dynamics. Japan: Yokohama; 2004. p. 12.

[32] Zhang S, Li X, Zhu Z. Numerical simulation of cryogenic cavitating flow by an extended transport-based cavitation model with thermal effects. Cryogenics. 2018;92:98–4.

[33] Shaheed R, Mohammadian A, Kheirkhah Gildeh H. A comparison of standard k–ε and realizable k–ε turbulence models in curved and confluent channels. Environ Fluid Mech. 2018;19(2):543–68.

[34] He Z, Guan W, Wang C, Guo G, Zhang L, Gavaises M. Assessment of turbulence and cavitation models in prediction of vortex induced cavitating flow in fuel injector nozzles. Int J Multiph Flow. 2020;157:104251.

[35] Qiao Z, Wang Z, Zhang C, Yuan S, Zhu Y, Wang J. PVAm–PIP/PS composite membrane with high performance for CO_2/N_2 separation. AIChE J. 2012;59(4):215–28.

[36] Patankar SV. Numerical heat transfer and fluid flow. Washington DC: Taylor & Francis; 2018.

[37] Jalayer M, Orsenigo C, Vercellis C. Fault detection and diagnosis for rotating machinery: A model based on convolutional LSTM, Fast Fourier and continuous wavelet transforms. Comput Ind. 2021;125:103378.